

# Controllable Synthesis of COFs-Based Multicomponent Nanocomposites from Core-Shell to Yolk-Shell and Hollow-Sphere Structure for Artificial Photosynthesis

Mi Zhang, Jia-Nan Chang, Yifa Chen, Meng Lu, Tao-Yuan Yu, Cheng Jiang, Shun-Li Li, Yue-Peng Cai, and Ya-Qian Lan\*

The precise tuning and multi-dimensional processing of covalent organic frameworks (COFs)-based materials into multicomponent superstructures with appropriate diversity are essential to maximize their advantages in catalytic reactions. However, up to now, it remains an ongoing challenge for the precise design of COFs-based multicomponent nanocomposites with diverse architectures. Herein, a metal organic framework (MOF)-sacrificed in situ acid-etching (MSISAE) strategy that enables continuous synthesis of core-shell, yolk-shell, and hollow-sphere COFs-based nanocomposites through tuning of core decomposition ( $\text{NH}_2\text{-MIL-125}$  into  $\text{TiO}_2$ ) rate is developed. More importantly, due to the multiple active sites, fast transfer of carriers, increased light utilization ability, et al, one of the obtained samples,  $\text{NH}_2\text{-MIL-125/TiO}_2\text{@COF-366-Ni-OH-HAc}$  (yolk-shell) with special three components, exhibits high photocatalytic  $\text{CO}_2$ -to-CO conversion efficiency in the gas-solid mode. The MSISAE strategy developed in this work achieves the precise morphology design and control of multicomponent hybrid composites based on COFs, which may pave a new way in developing porous crystalline materials with powerful superstructures for multifunctional catalytic reactions.

The natural photosynthesis process is the best example of harnessing  $\text{CO}_2$  in the air as a carbon source and utilizing renewable sunlight as powder source to transform  $\text{CO}_2$  and  $\text{H}_2\text{O}$  into carbohydrates and  $\text{O}_2$ .<sup>[3]</sup> Encouraged by the above procedure, immense efforts have been devoted to realizing the artificial photosynthesis, that is, photocatalytic  $\text{CO}_2$  reduction coupled with  $\text{H}_2\text{O}$  oxidation.<sup>[4]</sup> However, the accomplishment of artificial photosynthesis within single component catalyst system remains a great challenge. The main challenge lies in that the efficient integration of reduction and oxidation active sites in such photocatalyst system is hard to achieve and the rapid carriers recombination tendency is difficult to avoid.<sup>[5]</sup> To this end, multicomponent heterojunction materials with appropriate diversity and complex morphologies possess much potential in accomplishing the artificial photosynthesis, which attributes to their

## 1. Introduction

With increasing attention to the global problems of energy shortage and environmental pollution, finding renewable energy sources to replace fossil fuels has become one of the most urgent targets for human society.<sup>[1]</sup> Photocatalytic reduction of  $\text{CO}_2$  is regarded as an effective way for mitigation of the global warming and generation of renewable energy sources.<sup>[2]</sup>

accessible features including multiple active sites,  $\text{CO}_2$  enrichment, and fast separation of carriers through the selective integration of various functional materials.<sup>[6]</sup> Therefore, the rational design of multicomponent nanocomposites with proper functionality may be a favorable approach to realize the efficient artificial photosynthesis, yet this field is still at the early stage and there are tremendous efforts need to be made.

Covalent organic frameworks (COFs), a class of emerging crystalline porous organic materials, have been developed as promising photocatalysts because of their large surface area, well-defined porosity, and high light absorption capacity, etc.<sup>[7]</sup> Nonetheless, the applications of COFs-based materials in artificial photosynthesis are still rare, possibly due to the difficulty in design of COFs structures with multi-functionality or the lack of feasible strategy to explore COFs-based powerful photocatalyst systems. In previously reported works, COFs-based nanocomposites have been prepared to enrich the functionality of COFs by combining COFs with distinct functional materials, such as metal oxide, carbon materials, and metal organic framework (MOFs), which could not only possess the structural qualities of individual components but also afford novel properties.<sup>[8]</sup> Up to date, several kinds of COFs-based nanocomposites with core-shell morphology, including  $\text{Fe}_3\text{O}_4\text{@TpBD}$ ,<sup>[9]</sup> rGO

M. Zhang, M. Lu, Y.-P. Cai, Y.-Q. Lan  
School of Chemistry  
South China Normal University  
Guangzhou 510006, China  
E-mail: yqlan@njnu.edu.cn; yqlan@m.scnu.edu.cn

J.-N. Chang, Y. Chen, T.-Y. Yu, C. Jiang, S.-L. Li  
Jiangsu Collaborative Innovation Centre of Biomedical Functional Materials  
School of Chemistry and Materials Science  
Nanjing Normal University  
Nanjing 210023, China

 The ORCID identification number(s) for the author(s) of this article can be found under <https://doi.org/10.1002/adma.202105002>.

DOI: 10.1002/adma.202105002

(5%)-TpPa-1-COF,<sup>[10]</sup> and NH<sub>2</sub>-MIL-68-MOF@TPA-COF,<sup>[11]</sup> have been synthesized and successfully applied for phototherapy, photocatalytic H<sub>2</sub> evolution, and degradation of rhodamine dyes, respectively. However, the controllable syntheses of COFs-based multicomponent nanocomposites with other morphologies like yolk-shell or hollow-sphere still remain undeveloped and these nanocomposites are rarely explored their potential applications in artificial photosynthesis.<sup>[12]</sup> As we all known, the morphologies of nanomaterials have significant influences on their features and functions.<sup>[13]</sup> In this regard, COFs-based multicomponent nanocomposites with specially designed morphologies (e.g., yolk-shell or hollow-sphere morphology) might have the following features serving as photocatalysts: 1) the special shells permit multiple reflections of the incident light, thereby improving the light utilization;<sup>[14]</sup> 2) different components of COFs-based nanocomposites would accomplish the multi-step catalytic reactions such as photocatalytic CO<sub>2</sub> reduction and H<sub>2</sub>O oxidation reactions in one catalytic system;<sup>[15]</sup> 3) the diverse and tunable compositions make it possible to fabricate heterojunction to improve charge transfer and separation efficiency;<sup>[16]</sup> 4) more exposed active sites might be beneficial for the improvement of photocatalytic performance than that of bulk COFs-based nanocomposites.<sup>[17]</sup> Despite that, it is still long-sought-after that developing a feasible strategy for the rational design of COFs-based multicomponent nanocomposites with desired morphology is applicable in artificial photosynthesis.

Herein, for the first time, we develop a MOF-sacrificed in situ acid-etching (MSISAE) strategy to achieve the controllable syntheses of the uniform and monodisperse core-shell MOFs@COFs, yolk-shell MOFs/TiO<sub>2</sub>@COFs, and hollow-sphere TiO<sub>2</sub>@COFs nanocomposites through a facile solvothermal reaction. Different from the template-assisted methods reported previously, which generally contain multi-step synthesis procedures and sophisticated template removal processes, the MSISAE strategy has much superiority.<sup>[18]</sup> In the strategy, the core MOFs (NH<sub>2</sub>-MIL-125) of MOFs@COFs will undergo different etching degrees along with generating nano-sized TiO<sub>2</sub> through precisely tuning the content of acetic acid (HAc), reaction time, and reaction temperature during the synthesis process. Consequently, COFs-based nanocomposites with diverse well-defined architectures and two/three components (including COFs, MOFs, and TiO<sub>2</sub>) are obtained. Specially, the unique yolk-shell structure with multi-components (NH<sub>2</sub>-MIL-125/TiO<sub>2</sub>@COF-366-Ni-OH-HAc with yolk-shell structure, denoted as MTCN-H (ys)) realizes the coexistence of Z-scheme and II type heterojunction as well as photocatalytic oxidation and reduction sites in one system, which is successfully applied as an effective photocatalyst with outstanding photocatalytic CO<sub>2</sub> reduction performance, much higher than the pure COFs, MOFs, TiO<sub>2</sub>, and other nanocomposites with other morphologies. Experiments and density functional theory (DFT) calculations reveal the advantage of the coexistence of distinctive three components and special yolk-shell morphology in the COFs-based photocatalyst for CO<sub>2</sub> reduction. Our work will offer new insights to the design and development of COFs-based multicomponent nanocomposites for artificial photosynthesis and also may pave a new way in exploring crystalline materials-based nanocomposites in photocatalysis.

## 2. Results and Discussion

### 2.1. Synthesis and Characterization of COFs-Based Multicomponent Nanocomposites with Diverse Architectures

Figure 1 illustrates the synthetic process of various COFs-based multicomponent nanocomposites with diverse well-defined architectures by a MSISAE strategy. First, NH<sub>2</sub>-MIL-125 nanocrystals were synthesized from titanium isopropoxide (Ti(OC<sub>4</sub>H<sub>9</sub>)<sub>4</sub>) and 2-aminoterephthalic acid (NH<sub>2</sub>-BDC), according to the reported literature.<sup>[19]</sup> This as-synthesized NH<sub>2</sub>-MIL-125 solid nanospheres show an average diameter of 200–500 nm (see the scanning electron microscope (SEM) image and transmission electron microscope (TEM) image in Figure S1, Supporting Information). The crystal structure of the produced NH<sub>2</sub>-MIL-125 is also confirmed by powder X-ray diffraction (PXRD) spectroscopy, which matches well with the simulated one (Figure S2, Supporting Information). And then, 2,5-dihydroxyterephthalaldehyde (DHA) and tetra(pamino-phenyl)porphyrin nickel (II) (TAPP-Ni) were introduced into a mixture of NH<sub>2</sub>-MIL-125 and o-dichlorobenzene/ethanol with different 6 M HAc dosage (100, 200, and 250 μL) and heated at 120 °C for 72 h.<sup>[20]</sup> As is known, NH<sub>2</sub>-MIL-125 are unstable under acid conditions due to their relatively weak metal–ligand bond strength.<sup>[21]</sup> Consequently, a series of NH<sub>2</sub>-MIL-125@COF-366-Ni-OH-HAc (core-shell), NH<sub>2</sub>-MIL-125/TiO<sub>2</sub>@COF-366-Ni-OH-HAc (yolk-shell), and TiO<sub>2</sub>@COF-366-Ni-OH-HAc (hollow-sphere) nanocomposites denoted as MCN-H (cs), MTCN-H (ys), and TCN-H (hs), respectively, were obtained.

PXRD patterns tests of the three COFs-based multicomponent nanocomposites with diverse architectures were conducted, and the patterns indicate the characteristic that NH<sub>2</sub>-MIL-125 was etched by different HAc dosages to varying degrees and gradually transformed into TiO<sub>2</sub> (Figure 2a–c). As for MCN-H (cs), MTCN-H (ys), and TCN-H (hs), the presence of characteristic diffraction peaks at 3.4° is attributed to the (100) faces of COF-366-Ni-OH which indicates the high crystallinity of COFs in these nanocomposites. With the increase of HAc dosage, it can be found that the diffractions (25.3°, 37.8°, 48.1°, 53.9°, and 62.8°) attributing to anatase TiO<sub>2</sub> (PDF-21-1272) are more and more obvious, whereas those for crystalline NH<sub>2</sub>-MIL-125 are gradually weakened. The well-defined COFs-based nanocomposites were further characterized by Fourier-transform IR spectrum. The peak at ≈1615 cm<sup>-1</sup> can be assigned to the typical stretching band for the –C=N, further proves the successful synthesis of COF-366-Ni-OH in these three COFs-based nanocomposites.<sup>[22]</sup> Moreover, the bands at 1430 and 1533 cm<sup>-1</sup> assigned to the symmetrical stretching vibration of carboxylate groups in NH<sub>2</sub>-MIL-125 show gradual weakening from MCN-H (cs) to TCN-H (hs) (Figure S3, Supporting Information).<sup>[23]</sup> X-ray photoelectron spectroscopy (XPS) measurements were also performed for the three distinct samples to reveal the chemical composition and valence state of each components. As shown in Figures S4–S6, Supporting Information, a series of peaks corresponding to Ti, Ni, O, C, and N in the survey spectrum indicate that these elements exist on the surface of these COFs-based nanocomposites. The high-resolution XPS spectra of Ti 2p and Ni 2p show two apparently characteristic peaks corresponding to the spin doublet of Ti 2p<sub>1/2</sub>,

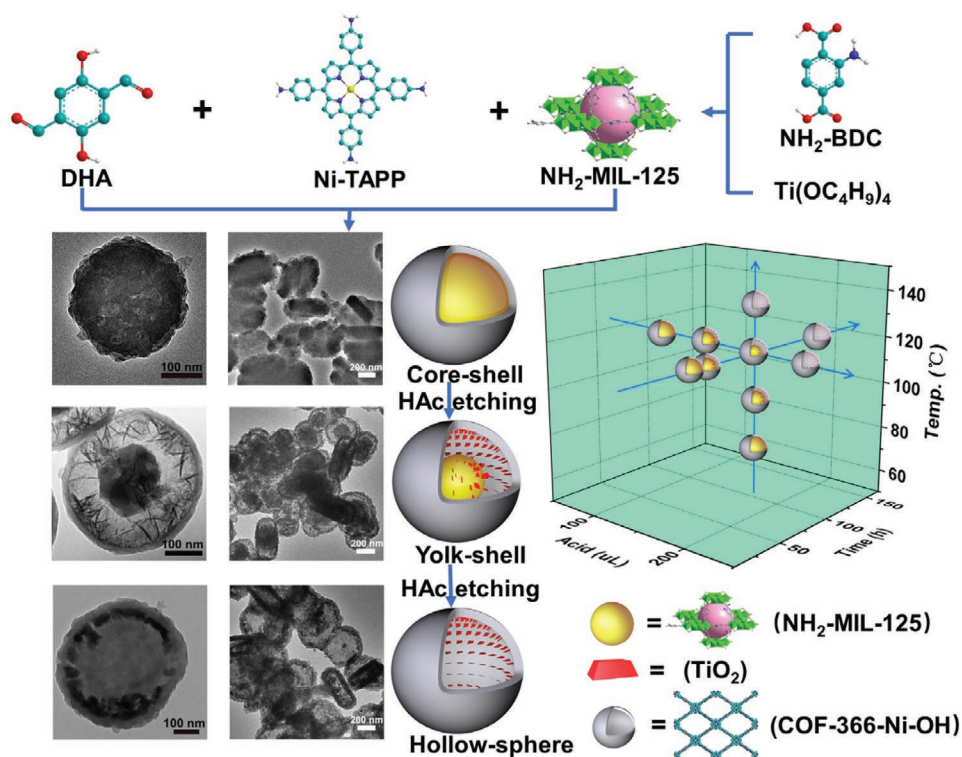


**Figure 1.** The schematic illustration of the formation of COFs-based multicomponent nanocomposites with diverse architectures.

Ti 2p<sub>3/2</sub> and Ni 2p<sub>1/2</sub>, Ni 2p<sub>3/2</sub>, respectively, which further certifies that the chemical state of COF-366-Ni-OH, NH<sub>2</sub>-MIL-125, or TiO<sub>2</sub> in these COFs-based nanocomposites.<sup>[24]</sup>

To further reveal the pattern of morphological changes of these COFs-based multicomponent nanocomposites via MSISAE strategy, a series of morphological studies were conducted by SEM and TEM tests. In contrast to the smooth surface of pristine NH<sub>2</sub>-MIL-125 (Figure S1, Supporting Information) and aggregated-nanosheets morphology of COF-366-Ni-OH (Figure S7, Supporting Information), the surface of NH<sub>2</sub>-MIL-125 is well covered by the vertically grown COFs nanosheets in MCN-H (cs) under the presents of 100 μL of the 6 M HAc dosage during the reaction (Figures 1 and 2). And then, the NH<sub>2</sub>-MIL-125 which corrodes from the outside toward the inside shows a yolk-shell morphology with the increase of the added HAc amount (Figure 1). Specifically, as the HAc dosage increases further to 250 μL, it is found that the entire yolk component has transformed into TiO<sub>2</sub> nanoparticle, which gathers at the inner surface of COFs shell and forms a hollow-sphere structure, as shown in Figure 1. However, the SEM images of these COFs-based nanocomposites prepared with different HAc dosage reveal that the nanosphere shape of NH<sub>2</sub>-MIL-125 is well retained during the etching process (inset of Figure 2a–c). The morphology changes from core-shell to yolk-shell and then to the hollow-sphere structure of the COFs-based nanocomposites, also confirmed by the high-angle annular dark-field scanning TEM (HAADF-STEM), the energy dispersive X-ray spectroscopy (EDX) line scanning spectra of Ti (yellow lines) and element mapping images (Figure 2). In the HAADF-STEM, several TiO<sub>2</sub> nanoparticles with an average size of 10–20 nm are observed

on the inner surface of COF-366-Ni-OH in MTCN-H (ys) and TCN-H (hs) (Figure 2e,f). The density of Ti for MTCN-H (ys) is the highest in the core region of nanosphere and decreases toward the edge, whereas some Ti is also detected on the inner surface of COF-366-Ni-OH (Figure 2e). In contrast, uniform distribution and a lower density of Ti are observed for MCN-H (cs) and TCN-H (hs), respectively (Figure 2d,f). The corresponding element mappings of N, Ni, O, and Ti (Figure 2g–i) suggest that these elements distribute uniformly throughout the series of COFs-based multicomponent nanocomposites. Specifically, the lattice fringe with a spacing 0.36 nm is assigned to the (101) plane of anatase TiO<sub>2</sub> in MTCN-H (ys) and TCN-H (hs) (Figure 2h,i), which further confirms the core MOFs have been corroded by HAc along with the generation of TiO<sub>2</sub>.

The porous characters of these as-prepared NH<sub>2</sub>-MIL-125, COF-366-Ni-OH, MCN-H (cs), MTCN-H (ys), and TCN-H (hs) were investigated by N<sub>2</sub> adsorption/desorption isotherm and pore size distribution. The adsorption isotherms show that the micropore amount of these COFs-based nanocomposites gradually decrease with raised HAc dosage (Figure S8a, Supporting Information). Moreover, mesoporosity becomes more noticeable confirmed by the pore size distribution data (Figure S8b, Supporting Information). This may be due to the local dissolution and defect generation within the core layer (NH<sub>2</sub>-MIL-125) after acid treatment.<sup>[25]</sup> The thermogravimetric analysis (TGA) of NH<sub>2</sub>-MIL-125, COF-366-Ni-OH, TiO<sub>2</sub>, TiO<sub>2</sub>/NH<sub>2</sub>-MIL-125, and three COFs-based multicomponent nanocomposites prepared at different HAc dosage under O<sub>2</sub> atmosphere are displayed in Figure S9, Supporting Information. The TGA proves

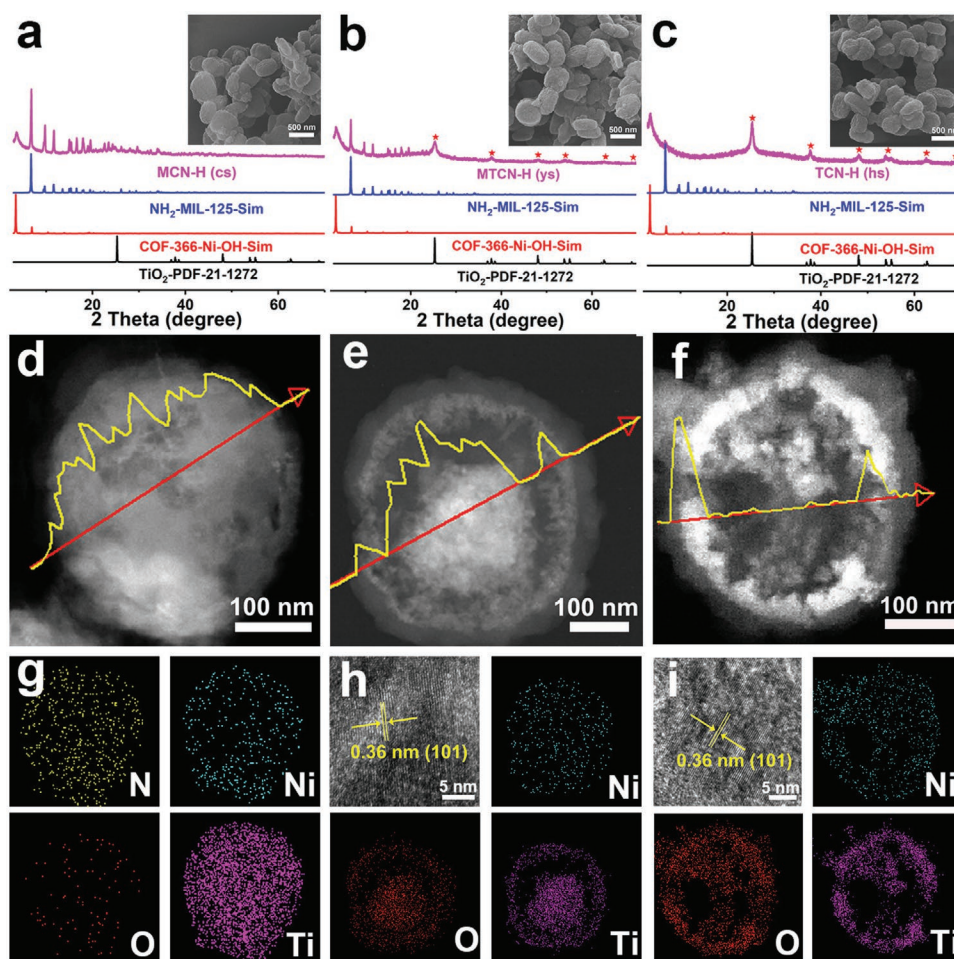


**Figure 2.** a–c) The PXRD, (inset of a–c) SEM, d–f) elementary line scanning spectra, g–i) EDX elemental mapping images and h,i) HAADF-STEM of COFs-based multicomponent nanocomposites prepared with different HAC dosage (from left to right: MCN-H (cs), MTCN-H (ys), and TCN-H (hs), ★ represents the peaks of TiO<sub>2</sub>).

that these COFs-based nanocomposites show thermal stability up to 300 °C, and the weight ratios of each component are calculated to be  $\approx 64.3 : 35.7$  (NH<sub>2</sub>-MIL-125 : COF-366-Ni-OH) for MCN-H (cs),  $16.7 : 33.8 : 49.5$  (NH<sub>2</sub>-MIL-125 : TiO<sub>2</sub> : COF-366-Ni-OH) for MTCN-H (ys), and  $36.1 : 63.9$  (TiO<sub>2</sub> : COF-366-Ni-OH) for TCN-H (hs), respectively.

In addition, we also manipulated the morphologies of COFs-based nanocomposites from core-shell and yolk-shell to hollow-sphere by tuning the reaction time and temperature through the MSISAE process (Figure 1). A series of NH<sub>2</sub>-MIL-125@COF-366-Ni-OH-Temperature (core-shell), NH<sub>2</sub>-MIL-125/TiO<sub>2</sub>@COF-366-Ni-OH-Temperature (yolk-shell), and TiO<sub>2</sub>@COF-366-Ni-OH-Temperature (hollow-sphere) denoted as MCN-Te (cs), MTCN-Te (ys), and TCN-Te (hs), respectively, are obtained, when these COFs-based nanocomposites were prepared at different reaction temperature (80, 120, and 140 °C, respectively). And, another series of heterojunction structures with different morphologies (denoted as MCN-Ti (cs), MTCN-Ti (ys), and TCN-Ti (hs)) were also obtained, when COFs-based nanocomposites were prepared at different reaction time (6, 72, and 144 h, respectively). SEM, TEM, and PXRD tests show that the increment of reaction time and temperature will also

increase the corrosion degree of NH<sub>2</sub>-MIL-125 and produce more TiO<sub>2</sub> nanoparticles, along with the change of morphology (Figures S10–S15, Supporting Information). To explore the versatility of the synthetic strategy, we also synthesized other NH<sub>2</sub>-MIL-125/TiO<sub>2</sub>@COFs hybrid materials with yolk-shell structures. When four different COFs, that is COF-366-Cu-OH, COF-366-OH, TPCOF-Ni, and TPECOF-Ni (Figures S16 and S17, Supporting Information), are used as the shell of the NH<sub>2</sub>-MIL-125/TiO<sub>2</sub>@COFs hybrids, the NH<sub>2</sub>-MIL-125/TiO<sub>2</sub>@COF-366-Cu-OH (ys), NH<sub>2</sub>-MIL-125/TiO<sub>2</sub>@COF-366-OH (ys), NH<sub>2</sub>-MIL-125/TiO<sub>2</sub>@TPCOF-Ni (ys) and NH<sub>2</sub>-MIL-125/TiO<sub>2</sub>@TPECOF-Ni (ys) hybrid materials are also successfully synthesized. In addition, we also look for other MOF (NH<sub>2</sub>-MIL-88A) as the core of COFs-based nanocomposites with yolk-shell morphology through this MSISAE strategy. Yolk-shell morphologies and three components (MOF: NH<sub>2</sub>-MIL-125 or NH<sub>2</sub>-MIL-88A; COFs: four kinds of COFs; metallic oxide: TiO<sub>2</sub> or Fe<sub>2</sub>O<sub>3</sub>) of the above other COFs-based nanocomposites are also well characterized by TEM and PXRD tests (Figures S18–S21, Supporting Information).

The incident photocurrent response and photoluminescence (PL) emission spectra of these COFs-based multicomponent

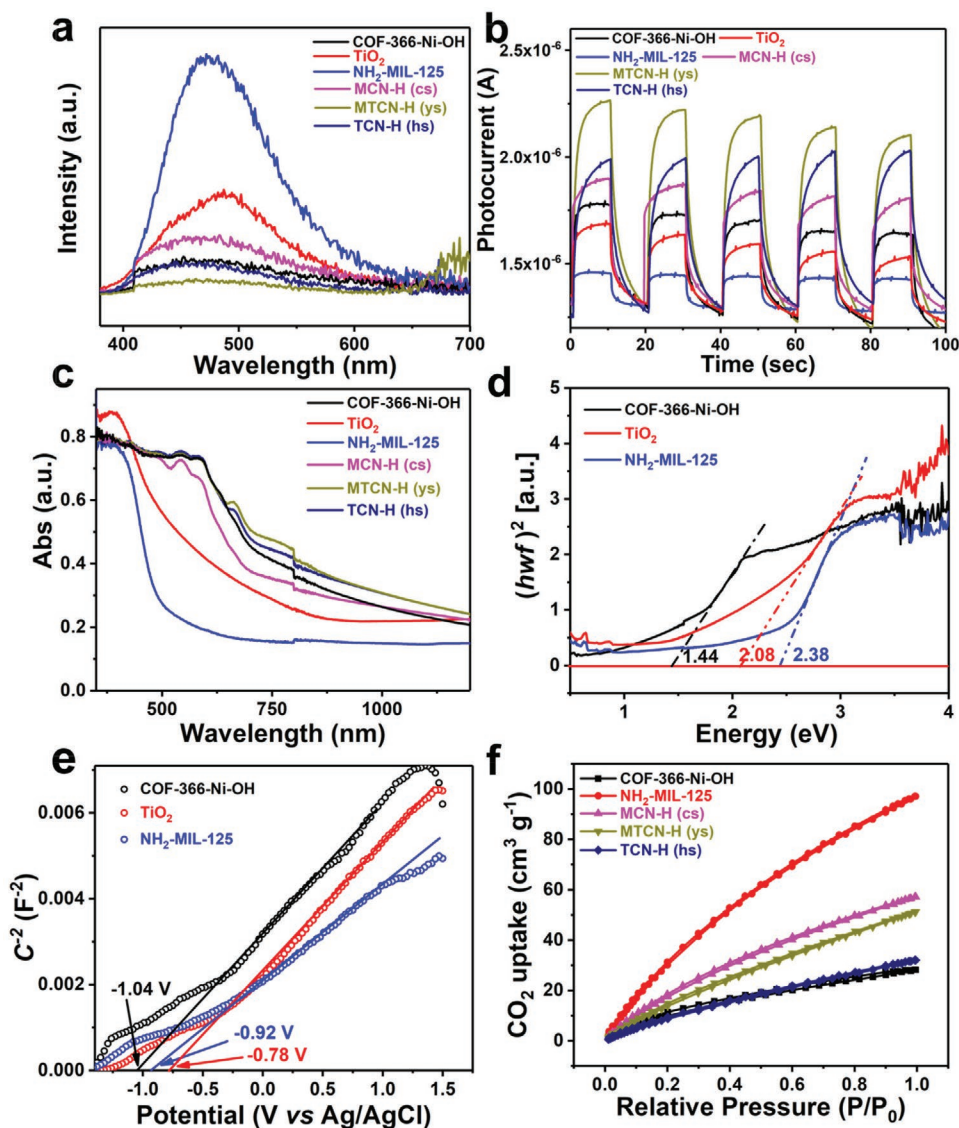


**Figure 3.** a) PL, b) transient photocurrent response, and c) solid-state UV–Vis absorption spectra of COF-366-Ni-OH, TiO<sub>2</sub>, NH<sub>2</sub>-MIL-125, and various COFs-based multicomponent nanocomposites prepared with different HAC dosage, d) Tauc plots of COF-366-Ni-OH, NH<sub>2</sub>-MIL-125, and TiO<sub>2</sub>, e) MS plots for COF-366-Ni-OH, NH<sub>2</sub>-MIL-125, and TiO<sub>2</sub>, f) CO<sub>2</sub> adsorption–desorption isotherm of NH<sub>2</sub>-MIL-125, COF-366-Ni-OH, and various COFs-based multicomponent nanocomposites prepared with different HAC dosage at 273 K.

nanocomposites and other control samples were tested to study the separation and migration of photogenerated electron–hole pairs. Taking COFs-based nanocomposites prepared with different HAC dosages for example, the MTCN-H (ys) behaves the lowest PL intensity and hence has the minimum recombination rate of photogenerated charge carriers compared with other samples (Figure 3a). In addition, as shown in Figure 3b, the order of photocurrent response intensity is MTCN-H (ys) > TCN-H (hs) > MCN-H (cs) > COF-366-Ni-OH > TiO<sub>2</sub> > NH<sub>2</sub>-MIL-125, which demonstrates that, among these six samples, MTCN-H (ys) has the largest number of photogenerated carriers with efficient separation. These above features are ascribed to the enhanced optical absorption of MTCN-H (ys), the effective separation of photogenerated carriers by TiO<sub>2</sub>/COF-366-Ni-OH and TiO<sub>2</sub>/NH<sub>2</sub>-MIL-125 heterojunction, and

its unique yolk-shell structure. To investigate the morphology-dependent photocatalytic properties of these COFs-based multicomponent nanocomposites, optical absorption properties of COF-366-Ni-OH, NH<sub>2</sub>-MIL-125, TiO<sub>2</sub>, MTCN-H (ys), TCN-H (hs) and MCN-H (cs) were investigated with the help of UV–Vis diffuse reflectance spectroscopy. As presented in Figure 3c, the COF-366-Ni-OH has an absorption edge at ≈600 nm. The optical absorbances of these COFs-based nanocomposites are close to that of the pure COF-366-Ni-OH which indicates that all of them have strong visible light absorption capability. The corresponding band gaps of TiO<sub>2</sub>, NH<sub>2</sub>-MIL-125, and COF-366-Ni-OH are calculated to be 2.08, 2.38, and 1.44 eV through the results of solid-state UV–Vis absorption spectra, respectively (Figure 3d). Mott–Schottky (MS) measurements were performed to calculate the electronic band positions of the

as-prepared materials (Figure 3e and Figure S22, Supporting Information). The conduction band (CB) positions are  $-0.84$ ,  $-0.72$ , and  $-0.58$  eV (vs normal hydrogen electrode) for COF-366-Ni-OH, NH<sub>2</sub>-MIL-125 and TiO<sub>2</sub> obtained by MS, respectively. Incorporated with the band gap of COF-366-Ni-OH, NH<sub>2</sub>-MIL-125, and TiO<sub>2</sub> from UV-Vis absorption data, the valence band (VB) positions of them can be determined as 0.60, 1.66, and 1.50 eV, respectively. In addition, it has been confirmed that high CO<sub>2</sub> adsorption capacity is conducive to improve the photocatalytic CO<sub>2</sub> reduction performance from the reported studies.<sup>[26]</sup> Thus, CO<sub>2</sub> uptake capacity tests were conducted for NH<sub>2</sub>-MIL-125, COF-366-Ni-OH and these COFs-based nanocomposites (Figure 3f). The results show that MTCN-H (ys) has higher CO<sub>2</sub> uptake at 273 K than COF-366-Ni-OH and TCN-H (hs), which is attributed to the presence of NH<sub>2</sub>-MIL-125.

## 2.2. Photocatalytic CO<sub>2</sub> Reduction Performance

Photocatalytic CO<sub>2</sub> reduction performances of these as-synthesized materials were explored with the gas-solid mode under the atmosphere of CO<sub>2</sub> and H<sub>2</sub>O vapor. Elaborated descriptions of the photocatalytic CO<sub>2</sub> reduction tests are given in the supporting information. The whole production of CO is  $\approx 67.49$   $\mu\text{mol g}^{-1}$  for MTCN-H (ys) after 4 h of successive illumination, which is significantly higher than that of MCN-H (cs) ( $\approx 5.78$   $\mu\text{mol g}^{-1}$ ), TCN-H (hs) ( $\approx 44.12$   $\mu\text{mol g}^{-1}$ ), and TiO<sub>2</sub> ( $\approx 13.17$   $\mu\text{mol g}^{-1}$ ) (Figure 4a,b). The value of MTCN-H (ys) is

comparable to those of reported COFs and MOFs-based photocatalysts for photocatalytic CO<sub>2</sub>-to-CO conversion with H<sub>2</sub>O oxidation (Table S1, Supporting Information). The CO yield is negligible for pure COF-366-Ni-OH and NH<sub>2</sub>-MIL-125 because the VB is too negative to oxidize H<sub>2</sub>O for the former and lack of suitable active sites to the reaction of H<sub>2</sub>O oxidation to O<sub>2</sub> for the latter.<sup>[27]</sup> The above results further support the superiority of MTCN-H (ys) with the unique morphology and ternary heterojunctions.

In addition, such special yolk-shell morphology and multi-components (COF-366-Ni-OH, NH<sub>2</sub>-MIL-125, and TiO<sub>2</sub>) display superior stability during a prolonged photocatalytic reaction for MTCN-H (ys). As shown in Figure 4c, the photocatalyst still maintains a good photocatalytic efficiency without an obvious declining trend after four cycles, indicating good durability of MTCN-H (ys). Concurrently, no significant changes are detected in the PXRD pattern, TEM, and SEM images before and after reaction, suggesting an excellent long-term photocatalytic stability for MTCN-H (ys) (Figures S23–S25, Supporting Information). Moreover, the source of catalytic products was determined by control photocatalytic experiments. First, when CO<sub>2</sub> ( $m/z = 44$ ) was replaced with <sup>13</sup>CO<sub>2</sub> ( $m/z = 45$ ) as reactant, apparent <sup>13</sup>CO ( $m/z = 29$ ) signal could be noticed in mass spectrum (Figure 4d). Second, when H<sub>2</sub>O was replaced by H<sub>2</sub><sup>18</sup>O, <sup>18</sup>O<sub>2</sub> ( $m/z = 36$ ) and <sup>18</sup>O<sup>16</sup>O ( $m/z = 34$ ) were discovered after the reaction (Figure S26, Supporting Information), confirming that the generated <sup>18</sup>O<sub>2</sub>/O<sub>2</sub> is derived from the oxidation of H<sub>2</sub><sup>18</sup>O/H<sub>2</sub>O.

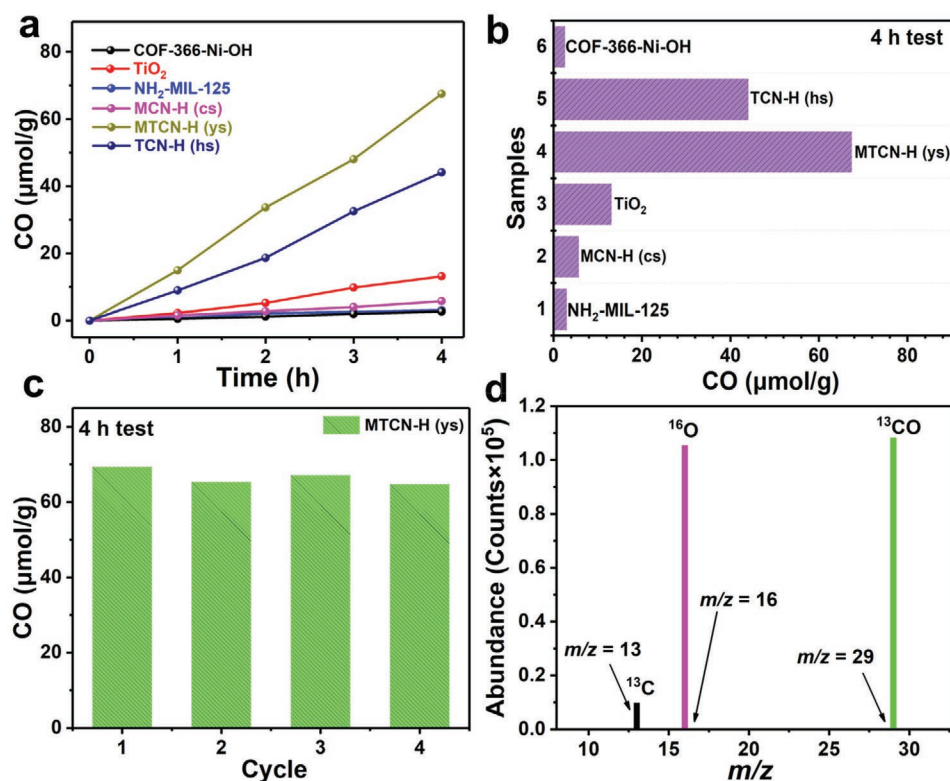


**Figure 4.** a) Time-dependent CO<sub>2</sub>-to-CO performances and b) photocatalytic CO<sub>2</sub>-to-CO performances for COF-366-Ni-OH, TiO<sub>2</sub>, NH<sub>2</sub>-MIL-125, and various COFs-based multicomponent nanocomposites prepared with different HAC dosage, c) durability measurements of MTCN-H (ys) (4 h test per cycle), d) Mass spectrum of <sup>13</sup>CO ( $m/z = 29$ ) produced from the photocatalytic reduction of <sup>13</sup>CO<sub>2</sub>.

### 2.3. Investigating Structure-Functional Relationships

According to the above performance tests and characterization results, we propose a rational photocatalytic mechanism based on the precise structure of the MTCN-H (ys) catalyst material. The in situ XPS test results show that the electrons can transfer from TiO<sub>2</sub> to COF-366-Ni-OH under photoexcitation in the heterojunction (Figure 5a), this results was also confirmed by theoretical calculation as shown below. Therefore, combining UV-Vis adsorption spectrum, MS, and in situ XPS tests, we can conclude that a Z-scheme heterojunction is formed between COF-366-Ni-OH and TiO<sub>2</sub>.<sup>[28]</sup> As shown in Figure 5b, under irradiation, both of COF-366-Ni-OH and TiO<sub>2</sub> can be excited to generate electrons and holes, after that the excited electrons of TiO<sub>2</sub> move to COF-366-Ni-OH and remain positive holes. As for NH<sub>2</sub>-MIL-125 and TiO<sub>2</sub>, they tend to form II-type heterojunction according to the literature previously reported.<sup>[29]</sup> The photogenerated electrons can migrate from the CB of NH<sub>2</sub>-MIL-125 to the CB of TiO<sub>2</sub>. Meanwhile, the photoinduced hole on VB of NH<sub>2</sub>-MIL-125 can migrate to VB of TiO<sub>2</sub>. As a result, the photogenerated electrons accumulate at the CB of COF-366-Ni-OH, then are used for CO<sub>2</sub> reduction. In the meantime, the holes accumulate at the VB of TiO<sub>2</sub> will be used for H<sub>2</sub>O oxidation on MTCN-H (ys) (Figure 5b). It is noted that the band gap of TiO<sub>2</sub> in this system is relative low (2.08 eV) compared to previously reported (3.2 eV). The possible reason is that the amine group ligand (NH<sub>2</sub>-BDC) which decomposed from NH<sub>2</sub>-MIL-125 and the surface states play an important role for reducing the band gap of TiO<sub>2</sub>. To check the above assumption,

we performed band structure calculations based on bulk, surface, and surface decorated TiO<sub>2</sub> by periodic models. As shown in Figures S27–S29, Supporting Information, the band gap of the surface decorated TiO<sub>2</sub> decreases ≈0.53 eV comparing with the bulk anatase TiO<sub>2</sub>, and the trend is consistent with our test results. The detail calculation results are shown on the below of Figure S27, Supporting Information. In MTCN-H (ys), a more negative CB value level than the CO<sub>2</sub>/CO standard reduction potential (−0.53 V vs RHE.) of COF-366-Ni-OH (−0.84 V vs RHE) and a more positive VB value of TiO<sub>2</sub> (+1.5 V vs RHE) than the H<sub>2</sub>O/O<sub>2</sub> standard oxidation potential (+0.82 V vs RHE) have been calculated by MS and UV-Vis absorption data which have proved that MTCN-H (ys) can catalyze the CO<sub>2</sub> reduction to CO with H<sub>2</sub>O as an electron donor.<sup>[30]</sup> The theoretical calculation of charge deformation density based on the MTCN-H (ys) with the effect of NH<sub>2</sub>-BDC ligand on TiO<sub>2</sub>, also supports the above proposed mechanism (Figure 5c and Figure S30, Supporting Information). The calculations show that the charge exchange occurs between COF-366-Ni-OH and TiO<sub>2</sub>. The CO<sub>2</sub> reduction pathway was studied by the computational hydrogen electrode model using DFT. The DFT calculation results show that the photocatalytic CO<sub>2</sub> reduction reaction is conducted on Ni metal center of TAPP on COF-366-Ni-OH. The detailed CO<sub>2</sub> to CO process is also shown in Figure S31, Supporting Information. In the photocatalytic process, the CO<sub>2</sub> molecule adsorbed at the Ni site is converted to CO after gradually gaining two electrons and two protons, simultaneously generating an H<sub>2</sub>O molecule. Among these elementary reaction steps, the adsorbed CO<sub>2</sub>\* on the TAPP-Ni and then accompanied by an electron transfer step

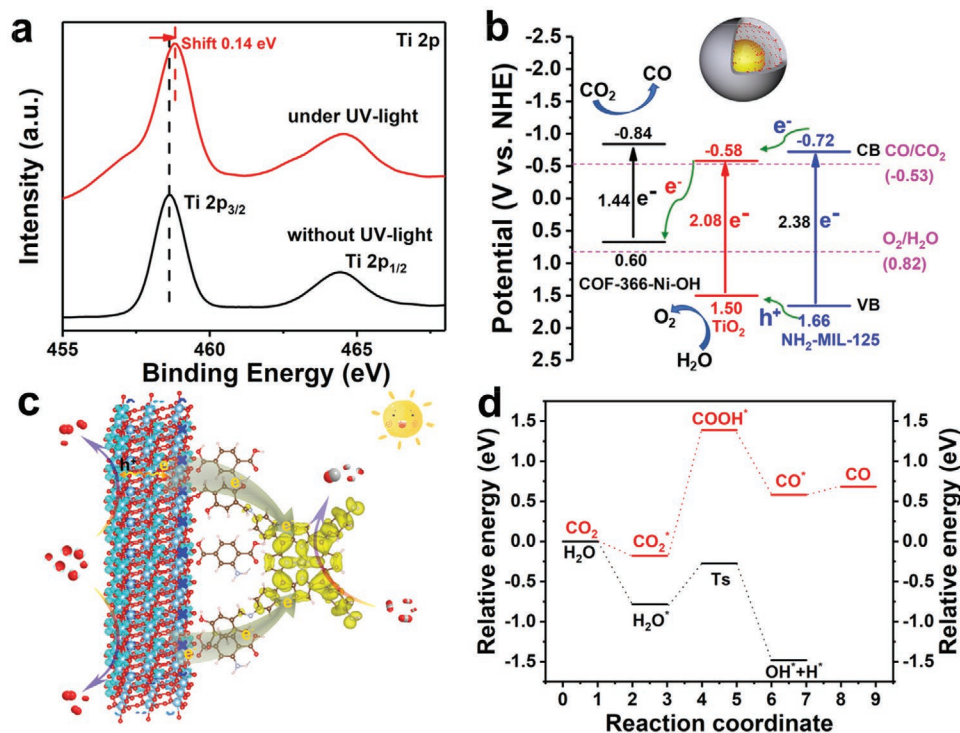


**Figure 5.** a) High-resolution in situ XPS for Ti 2p of TCN-H (hs) in the dark and under irradiation, b) schematic illustration of the charge-transfer process for MTCN-H (ys) under light irradiation, c) schematic of the mechanism for CO<sub>2</sub> reduction coupled with H<sub>2</sub>O oxidation for TiO<sub>2</sub> and COF-366-Ni-OH, d) DFT-calculated ΔG profiles of MTCN-H (ys) for the CO<sub>2</sub> to CO conversion and H<sup>+</sup> generation.

to generate COOH\* was calculated to be the rate-determining step based on thermodynamic Gibbs free energy calculation (Figure 5d, red curve). In this process, the produce and transfer of protons (H<sup>+</sup>) to CO<sub>2</sub>\* and COOH\* is another crucial step that affects the whole reaction rate.<sup>[31]</sup> Through theoretical calculations, we can find that NH<sub>2</sub>-MIL-125 facilitates the dissociation of H<sub>2</sub>O into H<sup>+</sup> (Figure 5d, black curve). Therefore, the NH<sub>2</sub>-MIL-125 in the center of the yolk-shell structure will make this micro-reactor at a higher H<sup>+</sup> concentration environment and therefore favor the H<sup>+</sup> participation in the CO<sub>2</sub> reduction reaction. The schematic energy-level diagrams of MCN-H (cs), TCN-H (hs), and MTCN-H (ys) are shown in Figure S32, Supporting Information. As can be seen, MCN-H (cs) lacks suitable active sites for the H<sub>2</sub>O oxidation and TCN-H (hs) possesses low CO<sub>2</sub> adsorption capability and less H<sup>+</sup> participating in the process of CO<sub>2</sub> reduction. In addition, compared with MCN-H (cs) and TCN-H (hs), MTCN-H (ys) has a longer lifetime of photogenerated carriers and suitable band gap position that can effectively separate photogenerated carriers and increase the optical absorption range attributing to the special ternary heterojunction systems and special yolk-shell morphology.

Overall, the improved performances can be attributed to the synergistic effect of the three components of MTCN-H (ys), as following: First, the special shells (COF-366-Ni-OH) permit multiple reflections of the incident light, thereby improving the light utilization; Second, the NH<sub>2</sub>-MIL-125 in the center of the yolk-shell structure will favor the H<sup>+</sup> participation in the CO<sub>2</sub> reduction reaction and enhance CO<sub>2</sub> adsorption capability; Third, TiO<sub>2</sub> is advantageous to the completion of H<sub>2</sub>O oxidation reactions. More importantly, the multivariate compositions (NH<sub>2</sub>-MIL-125, TiO<sub>2</sub>, and COF-366-Ni-OH) successfully fabricate the Z-scheme and II-type heterojunction simultaneously in one catalyst system, which is highly conducive to improve charge transfer and separation efficiency. Accordingly, MTCN-H (ys) shows excellent photocatalytic CO<sub>2</sub> reduction efficiency.

### 3. Conclusion

In summary, we present a MSISAE strategy that enables continuous syntheses of COFs-based heterojunction with core-shell, yolk-shell, and hollow-sphere structures through the precise tuning of core decomposition rate of NH<sub>2</sub>-MIL-125 into TiO<sub>2</sub> during the synthesis of COFs. The controllable collapse of NH<sub>2</sub>-MIL-125 core to in situ produce nano-size TiO<sub>2</sub> results in the controllable tuning of various morphologies with diverse multi-components. Thus, MTCN-H (ys) with rarely reported yolk-shell morphology displays remarkable catalytic performance in photocatalytic reduction of CO<sub>2</sub> with H<sub>2</sub>O, which can be ascribed to its unique yolk-shell architecture, distinctive three components and coexistence of Z-scheme and II type heterojunction supported by sufficient experimental results. Besides, we also study the mechanism for photoexcitation process and CO<sub>2</sub> reduction by combining experiments with theoretical calculations. The in situ XPS tests and DFT calculations prove that the photogenerated electrons driven by light effectively transfer from MOFs to TiO<sub>2</sub>, then to COFs, bringing about the electrons gathering at the Ni metal center in COFs and simultaneously used for the photocatalytic CO<sub>2</sub> reduction reaction. Meanwhile,

the positively charged holes in the TiO<sub>2</sub> fulfill the H<sub>2</sub>O oxidation reaction. Furthermore, NH<sub>2</sub>-MIL-125 facilitates the dissociation of H<sub>2</sub>O into H<sup>+</sup> and favors the H<sup>+</sup> participation step in the CO<sub>2</sub> reduction process, thus enhancing the CO<sub>2</sub> reduction performance. We believe that the controllable MSISAE strategy demonstrated in this work will provide novel inspirations for the rational design of porous crystalline materials based artificial photocatalysts.

### 4. Experimental Section

*The Synthesis of TAPP-Ni/Cu:* The synthesis of TAPP-Ni/Cu was carried out according to a previously published method.<sup>[32]</sup>

*The Synthesis of COF-366-Ni-OH:* The synthesis method of COF-366-Ni-OH followed previously reported procedure.<sup>[20]</sup> Specifically, TAPP-Ni (27 mg, 0.036 mmol), DHA (15.5 mg, 0.08 mmol), dichlorobenzene (1 mL), ethanol (1 mL), and 6 M aqueous HAc (200 μL) were mixed in a Pyrex tube (o.d × length, 19 × 65 mm). After sonication for ≈15 min, the tube was flash-frozen at 77 K and degassed to obtain an internal pressure of ≈100 mTorr. After the temperature returned to room temperature, the mixture was heated at 120 °C and kept it undisturbed for 72 h. After filtration and washed by tetrahydrofuran, the wet sample was transferred to a Soxhlet extractor and washed with tetrahydrofuran (12 h). Lastly, the product was evacuated at 120 °C under dynamic vacuum for 12 h to obtain an activated sample.

*The Synthesis of NH<sub>2</sub>-MIL-125:* The synthesis of NH<sub>2</sub>-MIL-125 was prepared through a method based on Nasalevich et al.<sup>[19]</sup>

*The Synthesis of TiO<sub>2</sub>:* NH<sub>2</sub>-MIL-125 (60 mg), dichlorobenzene (1 mL), ethanol (1 mL) and 6 M aqueous HAc (250 μL) were mixed in a Pyrex tube (o.d × length, 19 × 65 mm). And then, the subsequent treatment was similar to the synthesis of COF-366-Ni-OH.

*The Synthesis of COF-366-Ni-OH-Based Nanocomposites with Different Amount of HAc:* TAPP-Ni (27 mg, 0.036 mmol), DHA (15.5 mg, 0.08 mmol), NH<sub>2</sub>-MIL-125 (60 mg), dichlorobenzene (1 mL), ethanol (1 mL), and different amount of 6 M aqueous HAc (100, 150, 200, and 250 μL) were mixed in a Pyrex tube (o.d × length, 19 × 65 mm). The subsequent treatment was similar to the synthesis of COF-366-Ni-OH.

*The Synthesis of COF-366-Ni-OH-Based Nanocomposites with Different Time:* TAPP-Ni (27 mg, 0.036 mmol), DHA (15.5 mg, 0.08 mmol), NH<sub>2</sub>-MIL-125 (60 mg), dichlorobenzene (1 mL), ethanol (1 mL), and 6 M aqueous HAc (200 μL) were mixed in a Pyrex tube (o.d × length, 19 × 65 mm). Except that the mixture was heated at 120 °C and left undisturbed for 12, 24, 72, and 144 h, the subsequent treatment was similar to the synthesis of COF-366-Ni-OH.

*The Synthesis of COF-366-Ni-OH-Based Nanocomposites with Different Temperature:* TAPP-Ni (27 mg, 0.036 mmol), DHA (15.5 mg, 0.08 mmol), NH<sub>2</sub>-MIL-125 (60 mg), dichlorobenzene (1 mL), ethanol (1 mL), and 6 M aqueous HAc (200 μL) were mixed in a Pyrex tube (o.d × length, 19 × 65 mm). Except that the mixture was heated at 80, 100, 120, and 140 °C and left undisturbed for 72 h, the subsequent treatment was similar to the synthesis of COF-366-Ni-OH.

*The Synthesis of NH<sub>2</sub>-MIL-125/TiO<sub>2</sub>@COF-366-Cu-OH (ys) or NH<sub>2</sub>-MIL-125/TiO<sub>2</sub>@COF-366-OH (ys):* The synthesis of NH<sub>2</sub>-MIL-125/TiO<sub>2</sub>@COF-366-Cu-OH (ys) or NH<sub>2</sub>-MIL-125/TiO<sub>2</sub>@COF-366-OH (ys) was carried out following the same protocol as for MTCN-H (ys), by replacing the TAPP-Cu and TAPP with TAPP-Ni.

*The Synthesis of 2, 3, 6, 7-tetra (4-formylphenyl) Tetrathiafulvalene (TTF-4CHO):* TTF-4CHO was synthesized according to a previously published procedure.<sup>[5b]</sup>

*The Synthesis of NH<sub>2</sub>-MIL-125/TiO<sub>2</sub>@TTCOF-Ni (ys):* TAPP-Ni (15 mg, 0.02 mmol), TTF-4CHO (12.4 mg, 0.02 mmol), NH<sub>2</sub>-MIL-125 (40 mg), 1,4-dioxane (1 mL), 1,3,5-trimethylbenzene (1 mL), and 6 M aqueous HAc (100 μL) were mixed in a Pyrex tube (o.d × length, 19 × 65 mm). And then, the subsequent treatment is similar to the synthesis of COF-366-Ni-OH.

*The Synthesis of NH<sub>2</sub>-MIL-125/TiO<sub>2</sub>@TPECOF-Ni (ys):* TAPP-Ni (15 mg, 0.02 mmol), TPE (8.89 mg, 0.02 mmol), NH<sub>2</sub>-MIL-125 (40 mg), 1,4-dioxane (1 mL), 1,3,5-trimethylbenzene (1 mL), and 6 M aqueous HAc (100 μL) were mixed in a Pyrex tube (o.d × length, 19 × 65 mm). And then, the subsequent treatment is similar to the synthesis of COF-366-Ni-OH.

*The Synthesis of NH<sub>2</sub>-MIL-88A/Fe<sub>2</sub>O<sub>3</sub>@COF-366-Ni-OH (ys):* TAPP-Ni (27 mg, 0.036 mmol), DHA (15.5 mg, 0.08 mmol), NH<sub>2</sub>-MIL-88A (30 mg), dichlorobenzene (1 mL), ethanol (1 mL), and 6 M aqueous HAc (200 μL) were mixed in a Pyrex tube (o.d × length, 19 × 65 mm). And then, the subsequent treatment was similar to the synthesis of COF-366-Ni-OH.

## Supporting Information

Supporting Information is available from the Wiley Online Library or from the author.

## Acknowledgements

This work was financially supported by the NSFC (Grants 21871141, 21871142, 22071109, 21901122 and 2210050486), Natural Science Research of Jiangsu Higher Education Institutions of China (19KJB150011), a project funded by China Postdoctoral Science Foundation (Grants 2019M651873 and 2020M682747), the Applied Science and Technology Planning Project of Guangdong Province of China (Grant 2017B090917002) and Guangzhou Basic and Applied Basic Research Fund Project (Grant 202102020209). The authors thank the Shenzhen HUASUAN technology for the assistant of theoretical calculation.

## Conflict of Interest

The authors declare no conflict of interest.

## Data Availability Statement

Research data are not shared.

## Keywords

artificial photosynthesis, covalent organic frameworks, diverse architectures, multicomponent nanocomposites

Received: June 30, 2021

Revised: August 26, 2021

Published online: September 24, 2021

- [1] a) J. Albero, Y. Peng, H. García, *ACS Catal.* **2020**, *10*, 5734; b) S. J. Davis, K. Caldeira, H. D. Matthews, *Science* **2010**, *329*, 1330; c) C. Fan, X. Jiang, J. Chen, X. Wang, S. Qian, C. Zhao, L. Ding, D. Sun, Y. Tang, *Small Struct.* **2021**, *2*, 2000017.
- [2] a) Y. Zhang, B. Xia, J. Ran, K. Davey, S. Z. Qiao, *Adv. Energy Mater.* **2020**, *10*, 1903879; b) W. Tu, Y. Zhou, Z. Zou, *Adv. Mater.* **2014**, *26*, 4607; c) R.-X. Yang, Y.-R. Wang, G.-K. Gao, L. Chen, Y. Chen, S.-L. Li, Y.-Q. Lan, *Small Struct.* **2021**, *1*, 2000009.

- [3] H.-N. Wang, Y.-H. Zou, H.-X. Sun, Y. Chen, S.-L. Li, Y.-Q. Lan, *Coord. Chem. Rev.* **2021**, *438*, 213906.
- [4] a) Y. Zhao, G. I. N. Waterhouse, G. Chen, X. Xiong, L.-Z. Wu, C.-H. Tung, T. Zhang, *Chem. Soc. Rev.* **2019**, *48*, 1972; b) Y. Huang, P. Du, W.-X. Shi, Y. Wang, S. Yao, Z.-M. Zhang, T.-B. Lu, X. Lu, *Appl. Catal., B* **2021**, *288*, 120001.
- [5] a) S. Sato, T. Arai, T. Morikawa, K. Uemura, T. M. Suzuki, H. Tanaka, T. Kajino, *J. Am. Chem. Soc.* **2011**, *133*, 15240; b) M. Lu, J. Liu, Q. Li, M. Zhang, M. Liu, J.-L. Wang, D.-Q. Yuan, Y.-Q. Lan, *Angew. Chem., Int. Ed.* **2019**, *58*, 12392.
- [6] a) F. You, J. Wan, J. Qi, D. Mao, N. Yang, Q. Zhang, L. Gu, D. Wang, *Angew. Chem., Int. Ed.* **2020**, *59*, 721; b) C. Bie, B. Zhu, F. Xu, L. Zhang, J. Yu, *Adv. Mater.* **2019**, *31*, 1902868; c) X. Xu, X. Wang, *Small Struct.* **2020**, *1*, 2000009.
- [7] a) K. Geng, T. He, R. Liu, S. Dalapati, K. T. Tan, Z. Li, S. Tao, Y. Gong, Q. Jiang, D. Jiang, *Chem. Rev.* **2020**, *120*, 8814; b) X. Zhao, P. Pachfule, A. Thomas, *Chem. Soc. Rev.* **2021**, *50*, 6871; c) Y.-N. Gong, W. Zhong, Y. Li, Y. Qiu, L. Zheng, J. Jiang, H.-L. Jiang, *J. Am. Chem. Soc.* **2020**, *142*, 16723; d) Y. Qian, D. Li, Y. Han, H.-L. Jiang, *J. Am. Chem. Soc.* **2020**, *142*, 20763.
- [8] a) J. Fu, S. Das, G. Xing, T. Ben, V. Valtchev, S. Qiu, *J. Am. Chem. Soc.* **2016**, *138*, 7673; b) H. Peng, J. Raya, F. Richard, W. Baaziz, O. Ersen, A. Ciesielski, P. Samori, *Angew. Chem., Int. Ed.* **2020**, *59*, 19602; c) Y. Liu, W. Zhou, W. L. Teo, K. Wang, L. Zhang, Y. Zeng, Y. Zhao, *Chem* **2020**, *6*, 3172.
- [9] J. Tan, S. Namuangruk, W. Kong, N. Kungwan, J. Guo, C. Wang, *Angew. Chem., Int. Ed.* **2016**, *55*, 13979.
- [10] Y.-H. Yao, J. Li, H. Zhang, H.-L. Tang, L. Fang, G.-D. Niu, X.-J. Sun, F.-M. Zhang, *J. Mater. Chem. A* **2020**, *8*, 8949.
- [11] Y. Peng, M. Zhao, B. Chen, Z. Zhang, Y. Huang, F. Dai, Z. Lai, X. Cui, C. Tan, H. Zhang, *Adv. Mater.* **2018**, *30*, 1705454.
- [12] S. Wang, Y. Yang, P. Liu, Z. Zhang, C. Zhang, A. Chen, O. O. Ajao, B.-G. Li, P. Braunstein, W.-J. Wang, *Cell Rep. Phys. Sci.* **2020**, *1*, 100062.
- [13] a) Y. Wei, J. Wang, R. Yu, J. Wan, D. Wang, *Angew. Chem., Int. Ed.* **2019**, *58*, 1422; b) W. Wang, B. Xu, X. Pan, J. Zhang, H. Liu, *Angew. Chem., Int. Ed.* **2021**, *60*, 7802.
- [14] M. Liang, T. Borjigin, Y. Zhang, B. Liu, H. Liu, H. Guo, *Appl. Catal., B* **2019**, *243*, 566.
- [15] M. Zhang, M. Lu, Z.-L. Lang, J. Liu, M. Liu, J.-N. Chang, L.-Y. Li, L.-J. Shang, M. Wang, S.-L. Li, Y.-Q. Lan, *Angew. Chem., Int. Ed.* **2020**, *59*, 6500.
- [16] Y. Jiang, J.-F. Liao, H.-Y. Chen, H.-H. Zhang, J.-Y. Li, X.-D. Wang, D.-B. Kuang, *Chem* **2020**, *6*, 766.
- [17] S. Bao, J. Li, B. Guan, M. Jia, O. Terasaki, J. Yu, *Matter* **2020**, *3*, 498.
- [18] a) L. Liu, B. Zhang, X. Tan, D. Tan, X. Cheng, B. Han, J. Zhang, *Chem. Commun.* **2020**, *56*, 4567; b) M. Li, S. Qiao, Y. Zheng, Y. H. Andalousi, X. Li, Z. Zhang, A. Li, P. Cheng, S. Ma, Y. Chen, *J. Am. Chem. Soc.* **2020**, *142*, 6675.
- [19] M. A. Syzgantseva, C. P. Ireland, F. M. Ebrahim, B. Smit, O. A. Syzgantseva, *J. Am. Chem. Soc.* **2019**, *141*, 6271.
- [20] S. Kandambeth, D. B. Shinde, M. K. Panda, B. Lukose, T. Heine, R. Banerjee, *Angew. Chem., Int. Ed.* **2013**, *52*, 13052.
- [21] R. Bibi, H. Huang, M. Kalulu, Q. Shen, L. Wei, O. Oderinde, N. Li, J. Zhou, *ACS Sustainable Chem. Eng.* **2019**, *7*, 4868.
- [22] K. Li, N. K. Wong, M. J. Strauss, A. M. Evans, M. Matsumoto, W. R. Dichtel, A. Adronov, *J. Am. Chem. Soc.* **2021**, *143*, 649.
- [23] N. Li, X. Liu, J. Zhou, W. Chen, M. Liu, *Chem. Eng. J.* **2020**, *399*, 125782.
- [24] a) F. Xu, K. Meng, B. Cheng, S. Wang, J. Xu, J. Yu, *Nat. Commun.* **2020**, *11*, 4613; b) H. Lv, R. Sa, P. Li, D. Yuan, X. Wang, R. Wang, *Sci. China: Chem.* **2020**, *63*, 1289.
- [25] L. Luo, W.-S. Lo, X. Si, H. Li, Y. Wu, Y. An, Q. Zhu, L.-Y. Chou, T. Li, C.-K. Tsung, *J. Am. Chem. Soc.* **2019**, *141*, 20365.

- [26] S. Wang, M. Xu, T. Peng, C. Zhang, T. Li, I. Hussain, J. Wang, B. Tan, *Nat. Commun.* **2019**, *10*, 676.
- [27] J. Ran, M. Jaroniec, S.-Z. Qiao, *Adv. Mater.* **2018**, *30*, 1704649.
- [28] J. Low, B. Dai, T. Tong, C. Jiang, J. Yu, *Adv. Mater.* **2019**, *31*, 1802981.
- [29] L. Sun, Y. Yuan, F. Wang, Y. Zhao, W. Zhan, X. Han, *Nano Energy* **2020**, *74*, 104909.
- [30] R. Li, J. Hu, M. Deng, H. Wang, X. Wang, Y. Hu, H.-L. Jiang, J. Jiang, Q. Zhang, Y. Xie, Y. Xiong, *Adv. Mater.* **2014**, *26*, 4783.
- [31] J. Zhou, J.-X. Cui, M. Dong, C.-Y. Sun, S.-Q. You, X.-L. Wang, Z.-Y. Zhou, Z.-M. Su, *Chem. Commun.* **2020**, *56*, 7261.
- [32] S. Lin, C. S. Diercks, Y. B. Zhang, N. Kornienko, E. M. Nichols, Y. B. Zhao, A. R. Paris, D. Kim, P. Yang, O. M. Yaghi, C. J. Chang, *Science* **2015**, *349*, 1208.